PHYSICAL REVIEW B VOLUME 22, NUMBER 2 15 JULY 1980

Lateral interactions in rare gas monolayers: Band-structure models and photoemission experiments

K. Hermann and J. Noffke
Institut für Theoretische Physik B, Technische Universität Clausthal, 3392 Clausthal-Zellerfeld, West Germany and Sonderforschungsbereich 126, Clausthal, Göttingen, West Germany

K. Horn
Fritz-Haber-Institut der Max-Planck-Gesellschaft, 1000 Berlin 33, West Germany
(Received 20 December 1979)

The linear rigorous cellular (LRC) band-structure method is extended to the description of dispersion effects in two-dimensionally periodic systems. The method is used to calculate band structures of isolated hexagonal rare gas monolayers xenon to neon. The theoretical dispersion of krypton monolayers agrees well with an experimental band structure derived by angle-resolved photoemission for krypton physisorbed on Pd (100) presented here for the first time. For argon physisorbed on Pd (100) the measured separation of the bands at normal emission agrees fairly well with the theoretical separation at Γ. Further, data for xenon on Pd (100) published recently are also in good agreement with our theoretical results.

I. INTRODUCTION

The electronic structure of a free atom or molecule is modified upon adsorption on a solid surface. The adsorbate orbitals may admix some substrate character due to the bonding interaction. The degree of mixing depends on the orbital and the mechanism and strength of the substrate-adsorbate bonding. At higher coverages, adsorbed particles may additionally exhibit interaction with each other either directly (through space) or indirectly (through substrate). This leads in many cases to the formation of two-dimensional ordered overlayers. Because of the periodicity of the overlayer the electronic states of the adsorbate are then Bloch-type functions characterized by their two-dimensional wave vector $\vec{k}$ in the surface Brillouin zone (SBZ), and the electronic energy levels are bands in a two-dimensional band structure $\epsilon(\vec{k})$ rather than discrete levels of the free species.[1,2] Recently, two-dimensional band structures of atomic and molecular adsorbates on transition-metal surfaces have been measured using angular-resolved photoelectron spectroscopy (ARPES).[3-8] While band formation in adlayers has been theoretically predicted,[9] comparison of experiment with theory has been restricted to rather simple theoretical models[5,7,8] except for the case of oxygen on Al (111) in which a Korringa-Kohn-Rostoker (KKR) surface band-structure calculation using a jellium-type substrate was carried out.[10] It is desirable to compare experiment with other types of band-structure calculations in order to gain insight into the type and strength of the lateral interaction between the adsorbed particles.[4,6] If the adsorbate-substrate interaction is sufficiently weak, for example, in the case of physisorption of rare gases, the substrate has only little effect on the electronic structure of the adsorbate, and the dispersion of its electronic levels is predominantly determined by the direct lateral interaction. Physisorbed layers thus appear to be model systems for band calculations where only the isolated monolayer is considered, and the influence of the substrate on the adsorbate electronic structure is neglected. This concept has been successfully applied to the system xenon on Pd (100) (Refs. 4, 5), where the Xe $5p$ band disperison determined from ARPES data of the adsorbed layer was found to be in good agreement with the dispersion calculated in a simple tight-binding model for the isolated monolayer.

In the present paper, we compute the valence level dispersion of isolated hexagonal monolayers of xenon, krypton, argon, and neon using a layer version of the linear rigorous cellular (LRC) method.[11] As a test case, we compare our results for a xenon layer with the experimental dispersion curves obtained by Horn *et al.* for Xe : Pd (100).[4] For the case of a krypton layer, we compare theory with an experimental band structure derived from ARPES measurements of krypton on Pd (100) which are presented here for the first time. Our theoretical dispersion curves for isolated xenon and krypton monolayers agree well with the experimental band structures. In the case of argon on Pd (100), the energetic separation of two peaks observed in experiment agrees well with the values computed for the $3p$-derived bands at Γ for the isolated monolayer. Because of the inherent width of the Ar emission peaks which is of

similar magnitude compared to the extent of spin-orbit splitting and dispersion, it was not possible to unambiguously decompose the spectra into three $3p$-derived bands for different polar angles, and thus to determine an experimental band structure of this system. For neon, no measurements were carried out owing to the limitations of the present experimental setup.

The paper is organized as follows: in Sec. II we discuss the computational details. Section II A describes the geometries used in the calculations, while Sec. II B briefly outlines the layer LRC method. Section III gives some experimental details, and results and discussion are presented in Sec. IV.

II. COMPUTATIONAL DETAILS

A. Geometrical consideration

The electronic interaction within the adsorbed rare-gas monolayers is modeled by isolated monolayer films with hexagonal geometry. The nearest-neighbor distance of the Xe film d_{Xe} is taken from the experiment. Low-energy electron diffraction (LEED) data for Xe adsorbed on the Pd (100) surface indicate[12] that near saturation coverage two orthogonal domains with hexagonal structure are formed which are oriented along the Pd [010] and Pd [001] directions. The observed nearest-neighbor distance is $d_{Xe}=4.48$ Å (Ref. 12) being larger than the respective bulk value [$d=4.37$ Å (Ref. 18)] by about 3%. Hexagonal xenon overlayers with nearest-neighbor distances $d_{Xe}=4.4$–4.5 Å have been found for a number of different transition-metal substrates and surface orientations,[12–16] indicating that the substrate while determining the overall orientation of the monolayer has little influence on the adatom spacing. From LEED experiments it is found that Kr adsorbed on Ag (111) and Cu (211) surfaces[17] forms hexagonal overlayers with nearest-neighbor distances $d_{Kr}=4.19$ Å. This value being larger than the respective Kr bulk value [$d=4.04$ Å (Ref. 18)] by about 4% has been taken also in the model calculations. At present no LEED data for the Kr : Pd (100) system seem to be available. Ordered monolayers of Ar or Ne on transition-metal surfaces have not been studied so far but it seems plausible to assume hexagonal structures on the basis of the very weak van der Waals interactions involved in the formation of the adlayers. In the model calculations nearest-neighbor distances $d_{Ar}=4.03$ Å and $d_{Ne}=3.36$ Å are used which are larger than the respective Ar and Ne bulk value [$d=3.84$ Å for Ar,[18] 3.20 Å for Ne (Ref. 18)] by 5%. This seems to be a reasonable extrapolation from the results obtained for Xe and Kr.

B. Electronic structure

The electronic structure of the rare-gas monolayers is calculated using the LRC (linear rigorous cellular) band-structure method. This linearized version of the rigorous cellular method[20–22] has been successfully applied to various bulk systems[11] as well as to thin metal films.[23] Here we restrict ourselves to a discussion of the basic ideas of the method since the formalism is described in detail elsewhere.[11,23]

For the following let the z axis of the system be perpendicular to the hexagonal monolayer with $z=0$ defining the plane of the atomic nuclei. Then the elementary unit cell about each atom is a hexagonal prism whose planar faces A_i, $i=1,\ldots,6$ are perpendicular to the vectors

$$\vec{r}=\pm(1,0,0),\quad \vec{r}=\pm\left(\tfrac{1}{2},\sqrt{3}/2,0\right),\quad \vec{r}=\pm\left(-\tfrac{1}{2},\sqrt{3}/2,0\right)$$

at distances $\frac{1}{2}d$ from the atomic center, where d is the interatomic distance. This prism is divided into three cells, the "atomic" cell V_a about each nucleus where $z<\frac{1}{2}d$ and two empty cells V_{e1} and V_{e2} characterizing the vacuum region above and below the layer where $|z|>\frac{1}{2}d$, respectively.

The electronic states $\psi_{\vec{k}}(\vec{r})$ of the system are computed as approximate solutions of the one-electron equation

$$\mathcal{H}_{el}\psi_{\vec{k}}(\vec{r})=\epsilon(\vec{k})\psi_{\vec{k}}(\vec{r}) \tag{1}$$

in an effective one-electron potential $U(\vec{r})$ inside each cell and by imposing appropriate boundary conditions at the boundaries of adjacent cells as will be discussed in the following. Since the monolayer is assumed to be two-dimensionally periodic, the one-electron states $\psi_{\vec{k}}(\vec{r})$ can be classified by a two-dimensional wave vector $\vec{k}=(k_x,k_y)$ and the electronic energy spectrum $\epsilon(\vec{k})$ is represented as a two-dimensional band scheme.

The starting potential $U(\vec{r})$ of the system is computed from a linear superposition of free-atom charge densities $\rho_{atom}(\vec{r})$ about the respective atomic centers $\vec{R}_\mu$ of the layer

$$\rho_{layer}(\vec{r})=\sum_\mu \rho_{atom}(\vec{r}-\vec{R}_\mu), \tag{2}$$

where the self-consistent charge density of the free atom is obtained using the scalar relativistic approximation to Dirac's equation.[24,25] For the exchange-correlation part of the potential, Slater's approximation[26] is used, that is,

$$U_{xc}(\vec{r})=-3\alpha[(3/\pi)\rho_{layer}(\vec{r})]^{1/3}, \tag{3}$$

where the scaling factor α is chosen to be $\alpha=0.67$ for xenon, 0.70 for krypton, 0.72 for argon, and 0.73 for neon, quite close to the values proposed by Schwarz.[27] The starting potential of the system

has to be improved by iteration to self-consistency. However, in the case of rare-gas monolayers where strong charge deformations by covalent or metallic binding between the atoms do not occur, self-consistency is of minor importance and the starting potential represents already a very good approximation as will be discussed below.

The one-electron states $\psi_{\vec{k}}(\vec{r})$ of the system are represented in each cell by a linear combination of appropriate basis functions. Inside the atomic cell V_a the electronic potential $U(\vec{r})$ is, to a good approximation, spherically symmetric about the atomic center $\vec{R}_a$. Thus, for the computation of basis functions we replace the electronic potential $U(\vec{r})$ inside V_a by its spherical average (cf. Ref. 11)

$$\bar{U}_a(|\vec{r}-\vec{R}_a|)=\frac{1}{F_\bigcirc}\int\int_{\bigcirc\in V_a} U(\vec{r})d\Omega. \tag{4}$$

The solution of the scalar relativistic one-electron equation[25] for this averaged potential can be written as

$$\varphi_{lm}(\epsilon,\vec{r})=R_l(\epsilon,|\vec{r}-\vec{R}_a|)Y_{lm}(\hat{\vec{r}}-\hat{\vec{R}}_a), \tag{5}$$

where the radial part $R_l(\epsilon,r)$ for a given energy ϵ is computed from the radial equation

$$\left[-\Delta_r+\frac{l(l+1)}{r^2}+[\bar{U}_a(r)-\epsilon]\left(1-\frac{1}{c^2}[\bar{U}_a(r)-\epsilon]\right)-\frac{(d\bar{U}_a/dr)(r)(d/dr)}{c^2\{1-(1/c^2)[\bar{U}_a(r)-\epsilon]\}}\right]R_l(\epsilon,r)=0 \tag{6}$$

and the angular part $Y_{lm}(\hat{r})$ is a spherical harmonic.

The wave functions $\varphi_{lm}(\epsilon,\vec{r})$ define a basis set in cell V_a which serves for an expansion of the one-electron states $\psi_{\vec{k}}(\vec{r})$ of the system for a given energy ϵ, i.e.,

$$\psi_{\vec{k}}(\vec{r})=\sum_{l,m} c_{lm}\varphi_{lm}(\epsilon,\vec{r}) \tag{7}$$

inside V_a. In the rigorous cellular method[22] the energy dependence of the basis functions $\varphi_{lm}(\epsilon,\vec{r})$ is accurately accounted for, resulting in a nonlinear eigenvalue problem for the computation of the expansion coefficients c_{lm} and the energy values ϵ of the system. However, it is found in a number of systems[11] that the basis functions vary quite smoothly with energy. Within a range of ~0.5 Ry about a given trial energy ϵ_0 the energy dependence of $\varphi_{lm}(\epsilon,\vec{r})$ can be described approximately by its first-order Taylor expansion

$$\begin{aligned}\varphi_{lm}(\epsilon,\vec{r}) &\cong \varphi_{lm}(\epsilon_0,\vec{r})+(\partial/\partial\epsilon)\varphi_{lm}(\epsilon,\vec{r})|_{\epsilon=\epsilon_0}(\epsilon-\epsilon_0)\\ &=\varphi_{lm}(\epsilon_0,\vec{r})+\dot{\varphi}_{lm}(\epsilon_0,\vec{r})(\epsilon-\epsilon_0),\end{aligned} \tag{8}$$

suggesting that $\psi_{\vec{k}}(\vec{r})$ for energies ϵ within a reasonable range about ϵ_0 can be approximately described as

$$\psi_{\vec{k}}(\vec{r})=\sum_{l,m}[c_{lm}\varphi_{lm}(\epsilon_0,\vec{r})+d_{lm}\dot{\varphi}_{lm}(\epsilon_0,\vec{r})] \tag{9}$$

using a basis set $\{\varphi_{lm}(\epsilon_0,\vec{r}),\dot{\varphi}_{lm}(\epsilon_0,\vec{r})\}$ which does not vary with energy ϵ. Inside the empty cells V_{e1} and V_{e2} the electronic potential $U(\vec{r})$ varies quite strongly with distance z from the monolayer while its variation parallel to the layer is much smaller. Thus, for the computation of appropriate basis functions we replace $U(\vec{r})$ inside V_e by its planar average

$$\bar{U}_e(z)=\frac{1}{F_\diamondsuit}\int\int_{\diamondsuit\in V_e} U(\vec{r})dx\,dy. \tag{10}$$

Since the electron density inside the empty cells is quite small, relativistic effects become negligible and then we can restrict ourselves to basis functions which are computed using the nonrelativistic one-particle equation. For the averaged potential $\bar{U}_e(z)$ the solutions of the one-electron Schrödinger equation can be written as

$$\varphi_{\vec{G}}(\epsilon,\vec{r})=f_{\vec{G}}(\epsilon,z)e^{i(\vec{G}+\vec{k})\cdot\vec{r}_\parallel}, \tag{11}$$

where the normal part $f_{\vec{G}}(\epsilon,z)$ for a given energy is obtained from a one-dimensional Schrödinger equation

$$\{-d^2/dz^2+\bar{U}_e(z)-[\epsilon-(\vec{G}+\vec{k})^2]\}f_{\vec{G}}(\epsilon,z)=0. \tag{12}$$

Here $\vec{r}_\parallel=(x,y)$, $\vec{G}$ is a two-dimensional reciprocal lattice vector of the layer, and $\vec{k}$ is an arbitrary wave vector of the two-dimensional Brillouin zone. The solutions $\varphi_{\vec{G}}(\epsilon,\vec{r})$ define a basis set in cell V_e which serves for an expansion of the one-electron states $\psi_{\vec{k}}(\vec{r})$ of the system for a given energy ϵ, i.e.,

$$\psi_{\vec{k}}(\vec{r})=\sum_{\vec{G}} c^i_{\vec{G}}\varphi^i_{\vec{G}}(\epsilon,\vec{r}),\quad i=1,2 \tag{13}$$

inside V_{ei}. For the same reasons mentioned above we replace (13) by an expansion

$$\psi_{\vec{k}}(\vec{r})=\sum_{\vec{G}}[c^i_{\vec{G}}\varphi^i_{\vec{G}}(\epsilon_0,\vec{r})+d^i_{\vec{G}}\dot{\varphi}^i_{\vec{G}}(\epsilon_0,\vec{r})],\quad i=1,2 \tag{14}$$

where the basis functions do not vary with energy ϵ.

The coefficients c_{lm}, d_{lm}, and $c^i_{\vec{G}}$, $d^i_{\vec{G}}$ of (9) and (14) are determined in a two-step procedure. In a first step the coefficients are optimized such that different expansions from adjacent cells join smoothly at the respective cell boundaries and the

Bloch condition between adjacent atomic cells is valid [obviously expansions (14) guarantee that the Bloch condition between adjacent empty cells holds]. In a second step the coefficients are reoptimized such that $\psi_{\vec{k}}(\vec{r})$ is an approximate solution of the one-electron equation of the system yielding the respective one-electron energies $\epsilon(\vec{k})$. These two steps will be discussed in the following.

Since for computational reasons expansions (9) and (14) have to be truncated at some finite value $l_{\max}$ and $\vec{G}_{\max}$, respectively, the above boundary conditions cannot be satisfied rigorously. Thus we define an overall mismatch function

$$S^2 = \sum_m \int_{A_m} [|\psi^a_{\vec{k}}(\vec{r}+\vec{R}_m) - \psi^a_{\vec{k}}(\vec{r}) e^{i\vec{k}\cdot\vec{R}_m}|^2 + |\vec{n}_m\cdot\vec{\nabla}\psi^a_{\vec{k}}(\vec{r}+\vec{R}_m) - \vec{n}_m\cdot\vec{\nabla}\psi^a_{\vec{k}}(\vec{r}) e^{i\vec{k}\cdot\vec{R}_m}|^2] d\vec{\sigma}$$
$$+ \int_{A_{\text{top}}} [|\psi^a_{\vec{k}}(\vec{r}) - \psi^{e1}_{\vec{k}}(\vec{r})|^2 + |\vec{n}\cdot\vec{\nabla}\psi^a_{\vec{k}}(\vec{r}) - \vec{n}\cdot\vec{\nabla}\psi^{e1}_{\vec{k}}(\vec{r})|^2] d\vec{\sigma}$$
$$+ \int_{A_{\text{bottom}}} [|\psi^a_{\vec{k}}(\vec{r}) - \psi^{e2}_{\vec{k}}(\vec{r})|^2 + |\vec{n}\cdot\vec{\nabla}\psi^a_{\vec{k}}(\vec{r}) - \vec{n}\cdot\vec{\nabla}\psi^{e2}_{\vec{k}}(\vec{r})|^2] d\vec{\sigma}\,, \tag{15}$$

where $\psi^a_{\vec{k}}(\vec{r})$, $\psi^{e1}_{\vec{k}}(\vec{r})$, and $\psi^{e2}_{\vec{k}}(\vec{r})$ stand for the truncated expansions (9) and (14) of $\psi_{\vec{k}}(\vec{r})$ in the respective cells. The first part of S^2 represents the mismatch with respect to the Bloch condition of the expansion (9) and its derivative. The second and third part of S^2 represents the mismatch with respect to a smooth transition between empty-cell and atomic-cell expansions at the respective boundaries. A more detailed discussion of the mismatch function S^2 is given elsewhere.[22,11]

Minimization of S^2 with respect to all expansion coefficients under the constraint that the norm of the wave function be constant leads to linear eigenvalue equations depending on the trial energy ϵ_0.[22] However, within the LRC scheme it is assumed that expansions (9) and (14) for fixed ϵ_0 define a good basis for wave functions with energies about ϵ_0. So, for wave functions within a reasonable energy range about ϵ_0 the eigenvalue problem has to be solved only once for each wave vector $\vec{k}$. As a result of the eigenvalue problem one obtains sets of coefficients for different eigenvalues λ and hence functions $\psi^\lambda_{\vec{k}}(\vec{r})$ optimized with respect to the boundary conditions of the system. Since λ gives the magnitude of the mismatch function S^2 for $\psi^\lambda_{\vec{k}}(\vec{r})$ it can be used as a direct measure for the quality of the function. Obviously, the $\psi^\lambda_{\vec{k}}(\vec{r})$, given by expansions (9) and (14), do not solve the one-electron Schrödinger equation (1). Therefore, in the second step we determine approximate solutions $\psi_{\vec{k}}(\vec{r})$ of the one-electron equation as linear combinations of $\psi^\lambda_{\vec{k}}(\vec{r})$ for different λ:

$$\psi_{\vec{k}}(\vec{r}) = \sum_\lambda a_\lambda \psi^\lambda_{\vec{k}}(\vec{r})\,. \tag{16}$$

The coefficients a_λ are computed by minimizing the expectation value of the Hamiltonian $\mathcal{H}_{\text{el}}$. This variational problem leads to linear eigenvalue equations for the coefficients a_λ of the form

$$[\underline{H} - \epsilon(\vec{k})\underline{N}]\vec{a} = 0\,, \tag{17}$$

where $\underline{H}$ is the Hamiltonian matrix, $\underline{N}$ the overlap matrix, and $\vec{a}$ contains all coefficients a_λ. The numerical solution of Eqs. (17) yields the one-electron states $\psi_{\vec{k}}(\vec{r})$ and their energies $\epsilon(\vec{k})$ of the system.

In order to obtain good convergence of the basis functions $\psi^\lambda_{\vec{k}}(\vec{r})$ angular momentum expansions (9) inside V_a up to $l_{\max}=6$ and Fourier expansions (14) inside V_e with as many as seven $\vec{G}$ vectors are needed. Test calculations show that for the present systems the number of energy derivative basis functions $\dot{\varphi}_{lm}$ and $\dot{\varphi}^i_{\vec{G}}$ in (9) and (14) can be reduced to $l_{\max}=2$ and $\vec{G}=0$, respectively, without introducing serious errors. Altogether, in the first optimization step where the detailed spacial behavior of the wave function is important we obtain quite large matrices compared to those of other standard band-structure methods such as the linear combination of muffin-tin orbitals[28] (LMTO) or KKR.[29] However, in the second step, expansions (16) can be restricted to the seven smallest λ values in order to achieve good convergence of the energies resulting in quite small 7×7 eigenvalue matrices. Further, since here the wave function enters via volume integrals the angular momentum expansions (9) of the basis functions $\psi^\lambda_{\vec{k}}(\vec{r})$ computed in the first step can be truncated at $l_{\max}=2$ and the Fourier expansions (14) can be restricted to the $\vec{G}=0$ term without appreciable loss of accuracy in the energies.

The basis functions $\psi^\lambda_{\vec{k}}(\vec{r})$ in expansion (16) have been computed from numerical solutions of a one-electron equation using geometrical averages (4) or (10) of the potential $U(\vec{r})$ in each cell. However, in the second optimization step (17) the true non-muffin-tin potential $U(\vec{r})$ can be introduced into the matrix elements of the Hamiltonian ma-

trix quite easily, thus allowing for non-muffin-tin corrections beyond approximations (4) and (10). Since in rare-gas monolayers strongly directional covalent bonding between the atoms is very unlikely to occur, non-muffin-tin corrections beyond (4) and (10) are of minor importance and therefore can be neglected for the present purpose.

Obviously, the numerical solutions of the scalar relativistic one-electron equation[25] used for basis functions $\psi_{\vec{k}}^{\lambda}(\vec{r})$ inside V_a do not include corrections due to spin-orbit coupling which become quite important for elements as heavy as xenon. This effect is exactly accounted for if Dirac's fully relativistic one-electron equation is used instead of its scalar approximation. However, the use of spinors instead of scalar functions increases the size of the eigenvalue matrices considerably, thus making the calculation much more expensive in terms of computer time.[11] Therefore, in the present calculations the basis functions $\psi_{\vec{k}}^{\lambda}(\vec{r})$, requiring rather large expansions (9) and (14), are computed from numerical solutions of the scalar relativistic one-electron equation, whereas in the second eigenvalue problem (17), the energy optimization involving much smaller expansions (16), the spin-orbit coupling contribution is explicitly included in the Hamiltonian $\mathcal{H}$. The use of bispinor instead of scalar wave functions doubles the dimension of the eigenvalue matrix (17). This procedure has been found to yield results in good agreement with fully relativistic LRC calculations for bulk metals, e.g., lanthanum.[30]

Self-consistency of the band structure is achieved in an iterative procedure. In a first calculation the band structure $\epsilon^1(\vec{k})$ of the monolayer is determined as described above. The valence density of states $D(\epsilon)$ of the band structure $\epsilon^1(\vec{k})$ then follows from standard numerical routines.[31] Since the one-electron states $\psi_{\vec{k}}(\vec{r})$ described as (16) are given by expansions (9) inside the atomic cells V_a and (14) inside the empty cells V_e, one can decompose $D(\epsilon)$ into its angular momentum contributions $D_l(\epsilon)$ inside V_a and a contribution $D_{\text{out}}(\epsilon)$ of the two empty cells V_e where

$$D(\epsilon) = \sum_l D_l(\epsilon) + D_{\text{out}}(\epsilon) . \tag{18}$$

Integration of the different contributions between the bottom of the valence bands E_{bottom} and the Fermi energy E_F yields the respective fractional occupation numbers

$$q_l = \int_{E_{\text{bottom}}}^{E_F} D_l(\epsilon)d\epsilon , \quad q_{\text{out}} = \int_{E_{\text{bottom}}}^{E_F} D_{\text{out}}(\epsilon)d\epsilon \tag{19}$$

of the atom in the monolayer. In the present calculations we find that q_{out} is always small compared to the dominant angular momentum contributions q_l. Therefore q_{out} will be neglected in the following. In a second calculation the self-consistent charge density of the free atom with the above fractional occupations q_l is used to construct a new one-electron potential of the layer by linear superposition. For this potential a band structure $\epsilon^2(\vec{k})$ is computed from which new partial densities $D_l(\epsilon)$ and occupation numbers q_l follow. This procedure is repeated until the occupation numbers q_l from two successive iterations differ by less than 0.005.

III. EXPERIMENTAL

All measurements were performed with an ADES-400 ultrahigh-vacuum electron spectrometer (VG Scientific, Ltd.) mounted in a mu-metal vacuum chamber which was pumped by a Pfeiffer (Balzers) TPU 400 turbomolecular pump; after bake-out, base pressures of 5×10^{-11} torr were regularly obtained. The instrument allowed independent setting of the photon angle of incidence and electron emission angle. The analyzer acceptance window was situated in the plane of incidence of the light beam. The 5-cm-radius hemispherical electron energy analyzer was operated at a pass energy of 10 eV, energy resolution being about 200 meV. For the argon measurements, resolution was increased to 40 meV (2 eV pass energy). Photoelectrons were detected by a channeltron and recorded with the aid of a PDP-11 computer. The Pd (100) crystal, which was cut and polished to within $\frac{1}{2}^\circ$ of the desired orientation, was cleaned by oxygen treatment at high temperature, as well as by cycles of argon ion bombardment and annealing. It was mounted on a crystal holder which allowed cooling to 30 K using cold helium gas, or even lower using liquid He.[32]

IV. RESULTS AND DISCUSSION

A. Theoretical results

Figures 1–3 show the band structures of the Xe, Kr, Ar, and Ne monolayers computed by the formalism described in Sec. II. Here the valence energy levels $\epsilon(\vec{k})$ are given as a function of the wave vector $\vec{k}$ for characteristic paths within the two-dimensional surface Brillouin zone (SBZ) as shown in the insets of the respective figures.

There are always three different bands originating from the highest p orbitals of the respective atom ($5p$ for Xe, $4p$ for Kr, $3p$ for Ar, $2p$ for Ne). At $\Gamma(\vec{k}=0)$ the wave function of the energetically lowest band ϵ_1 is characterized by quantum numbers $j=\frac{1}{2}$, $m_j=\pm\frac{1}{2}$. The wave functions of the two energetically higher p bands at Γ are described

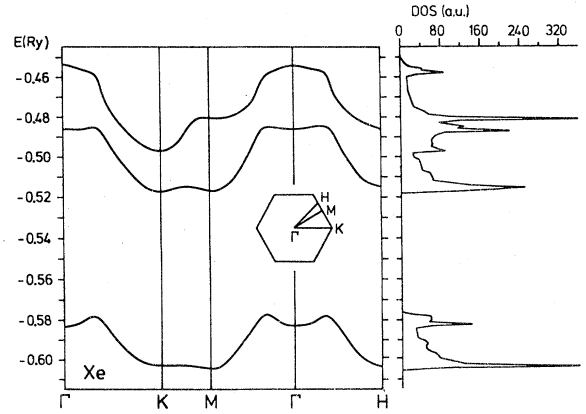

FIG. 1. Calculated band structure of an isolated hexagonal xenon monolayer along the main symmetry directions, as well as the direction ΓH. The SBZ is shown in the inset. In the right part the computed DOS is shown.

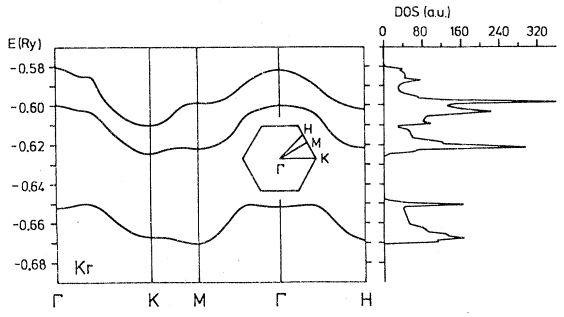

FIG. 2. Calculated band structure of an isolated hexagonal krypton monolayer.

by $j=\frac{3}{2}$, $m_j=\pm\frac{1}{2}$ (lower band ϵ_2) and $j=\frac{3}{2}$, $m_j=\pm\frac{3}{2}$ (higher band ϵ_3), respectively. For $\vec{k}$ vectors away from Γ the wave functions of the three bands admix quite small s- and d-type contributions as a consequence of the electronic interaction between neighboring atoms of the monolayer. However, for the present systems this interaction seems to be quite weak as the dispersion width of the three bands being a direct measure of the interatomic coupling turns out to be always rather small as can be seen from Table I.

The dispersion widths of Table I are quite strongly dependent on the interatomic spacing of the layer. If the nearest-neighbor distance of the xenon layer is increased by 10% from the experimental value, the calculated bandwidth of the $j=\frac{1}{2}$ band ϵ_1 reduces from 0.028 to 0.015 Ry. A decrease of the nearest-neighbor distance by 10% results in an increase in bandwidth from 0.028 to 0.057 Ry for ϵ_1. Thus, as expected, the interatomic interaction in the layer depends strongly on nearest-neighbor distance.

The energies of the three valence bands at Γ, $\epsilon_i(\Gamma)$, and the respective separations

$$\Delta\epsilon_1=\epsilon_2(\Gamma)-\epsilon_1(\Gamma)=\epsilon(j=\tfrac{3}{2},m_j=\pm\tfrac{1}{2},\Gamma)-\epsilon(j=\tfrac{1}{2},m_j=\pm\tfrac{1}{2},\Gamma),$$
$$\Delta\epsilon_2=\epsilon_3(\Gamma)-\epsilon_2(\Gamma)=\epsilon(j=\tfrac{3}{2},m_j=\pm\tfrac{3}{2},\Gamma)-\epsilon(j=\tfrac{3}{2},m_j=\pm\tfrac{1}{2},\Gamma)$$

are given in Table II for the four rare-gas monolayers. It is obvious from this Table that the energy separations $\Delta\epsilon_1$ and $\Delta\epsilon_2$ decrease monotonically from xenon to neon. This is to be expected for two reasons: first, spin-orbit interaction decreases with decreasing atomic number. Therefore the two high-lying and low-lying bands experience a successively smaller separation in going from xenon to neon. Secondly, the interatomic distances of the monolayers decrease much less with atomic number than the respective covalent radii. Thus, the valence orbitals of neigh-

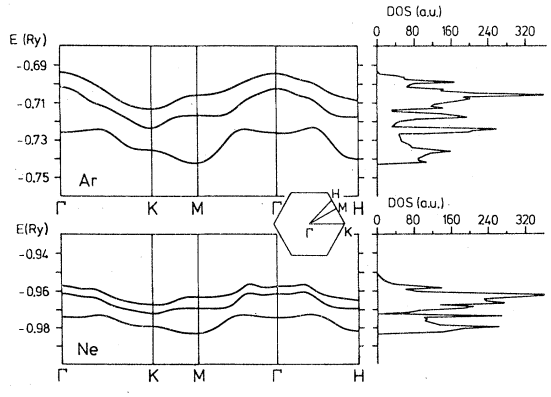

FIG. 3. Calculated band structures of isolated hexagonal argon and neon monolayers.

TABLE I. Computed dispersion width w_i for the three valence bands ϵ_i of the hexagonal rare-gas monolayers. Here w_i is defined as the energy range between the lowest and highest energy of the band ϵ_i. The energy values are given in Ry.

	w_1	w_2	w_3
Xe	0.028	0.034	0.043
Kr	0.023	0.026	0.032
Ar	0.019	0.022	0.019
Ne	0.010	0.012	0.017

TABLE II. Computed energies and energy separations of the three valence bands at Γ for the hexagonal rare-gas monolayers. For definitions of ϵ_i and $\Delta\epsilon_i$ see text.

	ϵ_1 (Γ) (Ry)	ϵ_2 (Γ) (Ry)	ϵ_3 (Γ) (Ry)	$\Delta\epsilon_1$ (Ry)	(eV)	$\Delta\epsilon_2$ (Ry)	(eV)
Xe	−0.583	−0.486	−0.454	0.097	1.32	0.032	0.44
Kr	−0.652	−0.600	−0.581	0.052	0.71	0.019	0.26
Ar	−0.726	−0.702	−0.694	0.024	0.33	0.008	0.11
Ne	−0.974	−0.961	−0.957	0.013	0.18	0.004	0.05

boring atoms in the layer will overlap less if the atoms become smaller, resulting also in a successively smaller separation between the valence bands in going from xenon to neon. The reduced overlap between valence orbitals also explains the decrease in dispersion width with decreasing atomic number as can be seen from Table I.

The right parts of Figs. 1–3 show the two-dimensional densities of states (DOS) of the respective monolayers computed with standard numerical methods[31] using 660 different $\vec{k}$ points in the full SBZ. Here, energies corresponding to small curvatures in the band schemes can be clearly identified as peaks in the DOS curves. A decomposition into angular momentum partial DOS reveals that the dominant contributions always come from p-type functions with s- and d-type admixtures being quite small as one would expect. Integration of the partial DOS curves over the valence energy range results in configurations of the atoms in the monolayers which are almost free-atom-like; they are given in Table III. This further substantiates the rather weak interaction between the atoms of the layers.

B. Experimental results and comparison

1. Xenon monolayers

The formation of hexagonal xenon overlayers on the Pd (100) surface has been studied recently by Horn *et al.*[4] using angular-resolved photoemission spectroscopy (ARPES). It has been shown[4,5] that the experimental dispersion curves can be described by a two-dimensional band scheme on the basis of a simple tight-binding method. Here, we use the ARPES data of the Xe : Pd (100) system as a test case to compare with our theoretical results using the LRC method.

TABLE III. Computed electronic configurations of the atoms in the monolayers. The fractional occupations are determined from the partial DOS curves of the respective band structures.

Xe	$5p^{5.92}$	$5d^{0.07}$	$6s^{0.01}$
Kr	$4p^{5.95}$	$4d^{0.04}$	$5s^{0.01}$
Ar	$3p^{5.97}$	$3d^{0.02}$	$4s^{0.01}$
Ne	$2p^{6.00}$		

In Fig. 4 our calculated band structure is compared to ARPES data obtained by Horn *et al.*[4,5] Xenon adsorbs on Pd (100) in a hexagonal layer with two domains orthogonal to each other. Thus, photoelectron spectra measured in any one azimuthal direction will be the sum of emission from the two domains, except in the unique direction labeled ΓH (corresponding to the [011] Pd azimuth) in the figure which is common to both domains, but does not represent a high symmetry direction. The calculated band dispersion for this direction is compared with experimental data in Fig. 4(a). Here the computed band scheme is rigidly shifted such that the value of the lower band ϵ_1 ($j = \frac{1}{2}$) coincides with the respective experimental value at Γ. This shift is introduced in order to account for local relaxation effects in the photoemission process that are not contained in the present calculations. For ΓH, good agreement of the theoretical dispersion curves with experiment is obtained for the whole range of $\vec{k}$ vectors ($\vec{k}$ vectors with $|\vec{k}| > 0.838$ Å^{-1} refer to $\vec{k}$ points outside the first

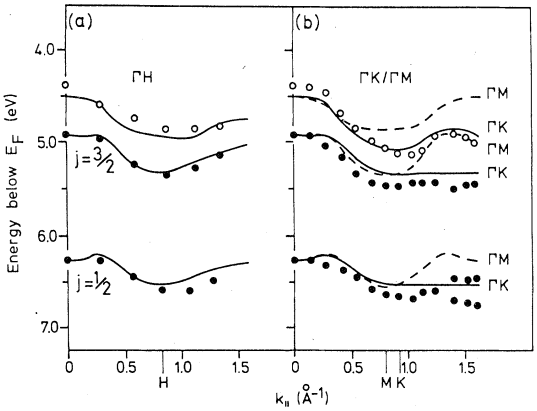

FIG. 4. Comparison between theoretical and experimental band structure for xenon along the ΓH direction (a) and the superimposed ΓK:ΓM directions (b). The appropriate quantum numbers for the Xe 5p states at Γ are shown in (a). The computed band scheme has been rigidly shifted such that the lowest band at Γ coincides with the experimental value.

surface Brillouin zone).

Good agreement between theory and experiment along ΓH in particular implies that the experimental separations between the bands at Γ, $\Delta\epsilon_1$, and $\Delta\epsilon_2$ (see Table II) are reproduced by our calculation. These band separations are strongly dependent on the interatomic separation of the xenon atoms. In test calculations, a reduction of the nearest-neighbor distance of the layer by 10% from the experimental value results in increased energy separations $\Delta\epsilon_1 = 1.57$ eV and $\Delta\epsilon_2 = 0.63$ eV, while an increase in interatomic distance by 10% results in $\Delta\epsilon_1 = 1.30$ eV and $\Delta\epsilon_2 = 0.24$ eV. Thus a fit of the computed band energy separations at Γ with the experimental values could be used to determine the nearest-neighbor distance of the adsorbed atoms; the LEED experiment, however, will be much more precise.

In Fig. 4(b) we compare the calculated band dispersions along ΓK and ΓM with experimental data for the [001] azimuth for the Xe : Pd (100) system in which ΓM and ΓK are superimposed due to the presence of the two orthogonal domains. For $\vec{k}$ vectors inside the first SBZ (i.e., for $|\vec{k}| < 0.81$ Å^{-1} in the ΓM and $|\vec{k}| < 0.935$ Å^{-1} in the ΓK direction) where the computed dispersions along ΓK and ΓM are almost identical, good agreement with the experimental data is obtained. While the low-lying band is clearly split outside the first SBZ in the experiment, due to the superposition of ΓM and ΓK, such splitting of the high-lying bands is not evident from the experimental band structure in Fig. 4(b). An inspection of the data presented in Fig. 1 of Ref. 5 gives the explanation: because of the inherent width and the small energy separation between the bands with ($j = \frac{3}{2}$, $m_j = \pm\frac{1}{2}$) and ($j = \frac{3}{2}$, $m_j = \pm\frac{3}{2}$), the spectral features are broadened and superimposed over each other for emission from outside the first SBZ. Here, one would expect to observe four bands in all (two for ΓK and two for ΓM), but the half-width of the peaks does not allow a clear distinction. The imporant result, however, is the good agreement inside the first SBZ.

2. *Krypton monolayer*

In Fig. 5 we show angle-resolved photoemission spectra of krypton physisorbed on Pd (100) at a crystal temperature of 50 K. These are the first photoemission data of krypton adsorbed on a transition-metal surface. The d band of palladium extends from E_F to about 4 eV below E_F, and the strong extra emission at about 6.5 to 8 eV is due to the adsorbed krypton. For normal emission ($\theta = 0°$) two peaks are observed at 7.55 and 6.7 eV below E_F, and a rather small peak at 6.35 eV below E_F. With increasing θ, all peaks shift to higher binding energies and the small peak at $\theta = 0°$ strongly increases in intensity. Unfortunately, no LEED data on the Kr : Pd (100) system are available at the present time. Since krypton forms a hexagonal layer on other transition-metal surfaces[14,17] with a nearest-neighbor distance only around 5% smaller than that of the respective xenon layer, we assume the Kr layer on Pd (100) to be hexagonal and oriented exactly in the same way as the xenon layer. Thus two orthogonal domains are assumed, with the ΓK and ΓM direction superimposed and oriented along the [001] Pd azimuth. The spectra can then be used to derive an experimental two-dimensional band structure using the procedure outlined elsewhere.[7] The experimental values for $\epsilon(\vec{k})$ are shown as dots and compared to the results of our calculations in Fig. 6. Again, the calculated band dispersion has been rigidly shifted to bring the energy of the lowest band at Γ in coincidence with the experimental value. Good agreement of the three dispersion curves along ΓH [see Fig. 6(a)] is obtained for the whole range of $\vec{k}$ vectors measured ($|\vec{k}| > 0.896$ Å^{-1} refers to $\vec{k}$ points outside the first SBZ). The experimental separation of the three bands at Γ, $\Delta\epsilon_1 = 0.80$ eV, and $\Delta\epsilon_2 = 0.38$ eV is reasonably well reproduced in the calculations (see Table II). Since there is some uncertainty about the value of the nearest-neighbor distance, and the calculated separation of the bands is strongly affected by this value, the small discrepancy between theory and experiment is not too disturbing.

Figure 6(b) compares the calculated band disper-

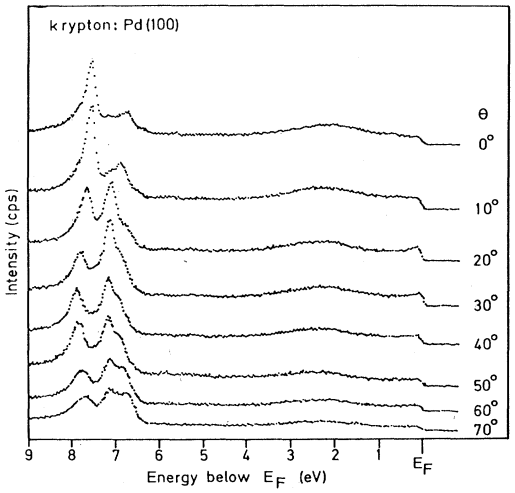

FIG. 5. Photoelectron spectra of krypton physisorbed on Pd (100) at 50 K for different polar angles of electron emission θ. Photon angle of incidence is 50°. Shifts in energetic position of the krypton $4p$-derived peaks around 6.5 to 8 eV below E_F are indicative of energy dispersion effects.

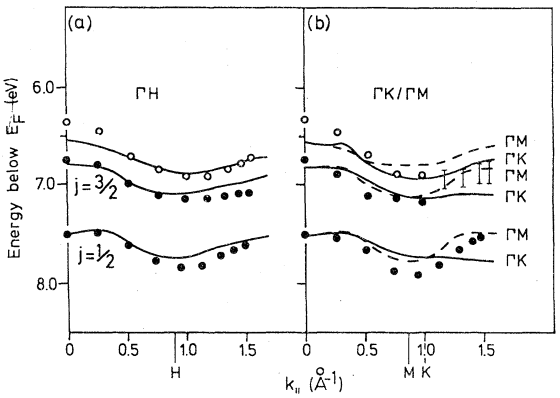

FIG. 6. Comparison of the calculated band structure for a hexagonal krypton monolayer (Fig. 2) with the experimental band structure derived from data shown in Fig. 5.

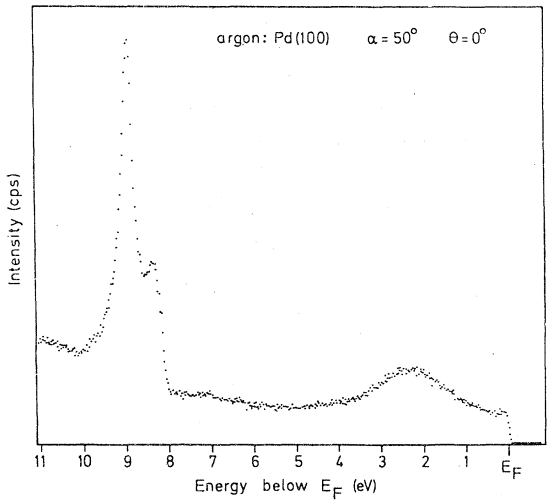

FIG. 7. Photoelectron spectrum of argon physisorbed on Pd (100) at 30 K. The two photoemission peaks due to the argon $3p$ levels are observed at 8.5 and 8.9 eV below E_F. Owing to the small separation, a splitting of the high-lying band into two components is not observed here.

sions along ΓK and ΓM with the experimental data for the [001] azimuthal direction. Again, we find good agreement between theory and experiment for $\vec{k}$ vectors inside the first Brillouin zone ($|\vec{k}| < 0.865$ Å^{-1} in the ΓM direction and $|\vec{k}| < 1.00$ Å^{-1} in the ΓK direction) where the computed dispersions of the three bands along ΓK and ΓM are almost identical. For larger $\vec{k}$ values, the emission due to the $j = \frac{3}{2}$ bands ϵ_2 and ϵ_3 cannot be well resolved into separate peaks owing to the problems discussed for xenon above; here, the width of the peaks near the top is indicated by bars in Fig. 6(b) for $\vec{k}$ values outside the first SBZ, and agrees well with the range covered by the four $j = \frac{3}{2}$ bands (two from the ΓK, two from the ΓM direction). The good overall agreement between the computed band structure and the measured dispersion suggests strongly that Kr adsorbs on Pd (100) in a hexagonal structure with a nearest-neighbor distance quite close to the value used in the calculation.

Thus our model calculations using the LRC method do agree well with the experimental band structure of xenon reported in the literature, as well as with the experimental band structure for krypton reported here for the first time. The calculations also reproduce well the energetic splitting of the Xe $5p$ and Kr $4p$ bands in the adsorbed phase.

3. *Argon monolayer*

Adsorption of argon on transition metals requires crystal temperatures below around 35 K because the physisorption energy is very small. An angle-resolved photoemission spectrum of Ar : Pd (100) is shown in Fig. 7, recorded at 30 K. It was taken at normal electron emission and a 50° angle of incidence, using He I (21.2 eV) radiation. We are not aware of any previously published photoemission or LEED results of argon adsorption on any transition-metal surface. Thus, we have to base our assumptions about the nearest-neighbor distance in this layer on a comparison of the measured energetic distance of the two peaks observed in Fig. 7 with the results of the LRC calculation. Since good agreement was found between theory and experiment for xenon and krypton, this is not a serious drawback.

Only two peaks are observed in the experimental spectrum. This can be understood by looking at the theoretical band structure shown in Fig. 3(a). The calculated splitting between the two $j = \frac{3}{2}$ bands is around 0.12 eV, too small to be resolved, considering the experimental half-width of the bands of around 0.25 eV. The spectrum for normal emission shows one peak at 8.90 and another at 8.50 eV below E_F. Interpreting the high energy peak as due to emission from the $j = \frac{1}{2}$ band ϵ_1, and the low energy peak due to the combined $j = \frac{3}{2}$ bands ϵ_2, ϵ_3, we get an experimental separation $\Delta\epsilon = 0.40$ eV which is in good agreement with the energetic separation $\overline{\Delta\epsilon} = 0.38$ eV calculated for a hexagonal monolayer. (Since we cannot experimentally separate ϵ_2 and ϵ_3, we have to take a mean value $\overline{\Delta\epsilon} = \Delta\epsilon_1 + \frac{1}{2}\Delta\epsilon_2$.) This indicates that the value used in our calculations for the nearest-neighbor distance is not too far off. A full comparison of the theoretical band structure will be possible when LEED and angle-resolved photoemission results at different polar angles are obtained. Such experiments as well as studies of a neon monolayer, which was not feasible with our experimental setup, are in preparation.

C. Conclusions

The above comparison has shown good agreement between two-dimensional band structures calculated by the LRC method and experimental band structures of rare-gas monolayers on Pd (100). These layers certainly present a unique opportunity to test layer band structure calculations, since the interaction with the surface can be neglected to a large extent. The inclusion of the geometric and electronic structure of the substrate into calculations using the LRC scheme should make this method also applicable to systems with strong adsorbate-substrate interaction, e.g., oxygen on aluminium (111) (Ref. 10) or sulfur on Pd (100).[33]

[1]A. M. Bradshaw and M. Scheffler, J. Vac. Sci. Technol. 16, 447 (1979).

[2]N. V. Richardson and A. M. Bradshaw, in *Electron Spectroscopy: Theory, Techniques and Applications*, edited by A. Baker and C. R. Brundle (Academic, London, 1980), Vol. 4.

[3]P. K. Larsen, N. V. Smith, M. Schlüter, H. H. Farrell, K. M. Ho, and M. L. Cohen, Phys. Rev. B 17, 2612 (1978).

[4]K. Horn, M. Scheffler, and A. M. Bradshaw, Phys. Rev. Lett. 41, 822 (1978).

[5]M. Scheffler, K. Horn, A. M. Bradshaw, and K. Kambe, Surf. Sci. 80, 69 (1979).

[6]K. Horn, A. M. Bradshaw, K. Hermann, and I. P. Batra, Solid State Commun. 31, 257 (1979).

[7]I. P. Batra, K. Hermann, A. M. Bradshaw, and K. Horn, Phys. Rev. B 20, 801 (1979).

[8]K. Jacobi and C. v. Muschwitz, Solid State Commun. 26, 477 (1978).

[9]A. Liebsch, Phys. Rev. B 17, 1653 (1978).

[10]P. Hofmann, C. v. Muschwitz, K. Horn, K. Jacobi, A. M. Bradshaw, M. Scheffler, and K. Kambe, Surf. Sci. 89, 327 (1979).

[11]L. Fritsche, M. Rafat, R. Glocker, and J. Noffke, Z. Phys. B 33, 1 (1979).

[12]P. W. Palmberg, Surf. Sci. 25, 598 (1971).

[13]M. A. Chesters and J. Pritchard, Surf. Sci. 28, 460 (1971).

[14]M. A. Chesters, M. Hussain, and J. Pritchard, Surf. Sci. 35, 161 (1973).

[15]A. Ignatiev, A. V. Jones, and T. N. Rhodin, Surf. Sci. 30, 573 (1972).

[16]Note, however, exceptions such as centered rectangular structures on Cu (110), Ag (110), and W (110) (Refs. 17, 19).

[17]R. W. Roberts and J. Pritchard, Surf. Sci. 54, 687 (1976).

[18]R. W. G. Wyckoff, *Crystal Structures* (Interscience, New York, 1964), 2nd ed., Vol. II.

[19]T. Engel, P. Bornemann, and E. Bauer, Surf. Sci. 81, 252 (1979).

[20]S. L. Altmann, in *Orbital Theories of Molecules and Solids*, edited by N. H. March (Clarendon, Oxford, 1974).

[21]L. Fritsche and M. Rafat, Lect. Notes Phys. 34, 97 (1975).

[22]J. Noffke, W. Brunn, and K. Hermann, Z. Phys. B 29, 353 (1978).

[23]J. Noffke, Ph.D. thesis, Technische Universität Clausthal, West Germany, 1979 (unpublished).

[24]D. D. Koelling and B. N. Harmon, J. Phys. C 10, 3107 (1977).

[25]H. Gollisch and L. Fritsche, Phys. Status Solidi B 86, 145 (1978).

[26]J. C. Slater, Phys. Rev. 81, 385 (1950).

[27]K. H. Schwarz, Phys. Rev. B 5, 2466 (1972).

[28]O. K. Andersen, Phys. Rev. B 12, 3060 (1975).

[29]See, e.g., B. Segall and F. S. Ham in *Methods in Computational Physics* (Academic, New York, 1968), Vol. 8.

[30]R. Glocker, private communication.

[31]We use a numerical routine developed by K. Hermann essentially along the lines of the method of Jepsen and Andersen. See also C. S. Wang and A. J. Freeman, Phys. Rev. B 19, 793 (1979).

[32]R. Unwin, K. Horn, and P. Geng (unpublished).

[33]K. Horn, N. V. Richardson, A. M. Bradshaw, and J. K. Sass, Solid State Commun. 32, 161 (1979).